Advanced Electronic Materials

www.advelectronicmat.de

RESEARCH ARTICLE OPEN ACCESS

An In-Line Machine Vision–Based Profilometry Tool for Non-Destructive Thickness Assessment of Perovskite Films

Juan Pablo Velásquez[1] | Juan José Patiño[1] | Keony Jimenez[1] | Santiago Mesa[1] | Milton Perez[1] | Ershad Parvazian[2] | Edwin Alexander Ramírez[1] | Rafael Betancur[1] | Trystan Watson[2] | Franklin Jaramillo[1]

[1]Center for Research, Innovation and Development of Materials–CIDEMAT, Faculty of Engineering, University of Antioquia–UdeA, Medellín, Colombia | [2]SPECIFIC IKC, Faculty of Science and Engineering, Swansea University, Fabian Way Swansea, UK

Correspondence: Juan Pablo Velásquez (juan.velasquez25@udea.edu.co) | Franklin Jaramillo (franklin.jaramillo@udea.edu.co)

Received: 10 December 2025 | **Revised:** 23 April 2026 | **Accepted:** 28 April 2026

Keywords: deep learning | In-line characterization | machine learning | machine vision | perovskite | roll-to-roll manufacturing | thickness inspection

ABSTRACT

Perovskite technology offers an advantage over conventional photovoltaics technologies related to its capacity to be manufactured on flexible substrates using continuous printing techniques, delivering an improved cost–benefit ratio. However, producing perovskite solar cells (PSCs) via these approaches demands rigorous quality control of printed films, as film uniformity influences device performance. This quality control process often involves characterization techniques, such as profilometry that is destructive, making them unsuitable for in-line real-time or large-scale inspections. Here, we present a versatile in-line inspection framework that combines a low-cost webcam-based transmitted-light imaging setup with a deep-learning regression model to estimate the thickness of printed $MAPbI_3$ and $FAPbI_3$ films in real time. The resulting prototype achieves coefficients of determination (R^2) of 0.985 and 0.986 and root-mean-square errors of 18 and 25 nm, respectively which is comparable to conventional invasive profilometry. When applied to 25 cm^2 flexible mini-modules, an inverse correlation between layer thickness variability and power conversion efficiency (PCE) was observed, and integrating the prototype into in-line inspection opened new possibilities for data-driven decision-making. This in-line, high-spatial-resolution inspection framework enables the fully automated and high-throughput manufacturing of large-area perovskite solar modules, by allowing real-time optimization of key operational parameters.

1 | Introduction

Over the past 10 years, PSCs have developed into highly efficient photovoltaic technology, fueled by a number of intrinsic characteristics of the light-absorbing materials themselves such as high absorption coefficient, low-cost fabrication, and low-temperature solution-processing capability [1, 2]. With the advancements in perovskite precursor chemistry [3], material composition [4–6], charge transport layer design [7], understanding of interfaces in multilayer structures [8, 9], and strategies for improving stability over the long term [10], additional enhancements in efficiencies at 27.3% for single-junction cells (active area: 0.058 cm^2) [11] and 30.1% for tandem devices (active area: 0.049 cm^2) [11] have been achieved in 2025. These values are significant, but they have only been achieved on small-area, laboratory-scale devices [12, 13]. Commercial scalability cannot be assumed solely based on high efficiencies, because they were achieved on limited-area devices [14]. Furthermore, while it can be argued that there is a technological limit to efficiency improvement due to intrinsic material properties, in practical terms the real scaling-up of solution-based deposition will limit increasing efficiency [15].

Most of these limitations arise from the difficulty in producing films that are both morphologically and functionally uniform in order to achieve consistent efficiency across the entire coated area and match the performance of small-area champion devices by reducing visible and performance-limiting defects [16–18]. Scaling up production of PSCs to a larger surface area involves challenges that are not encountered at the lab scale [19, 20]. In particular, various solution-based deposition techniques do not just need to be implemented at large areas at a high throughput (e.g., inkjet printing, blade coating, slot-die coating, bar coating, and gravure printing) but must also meet critical film quality and uniformity features over large surface areas [21–23]. The main challenge of these techniques is to produce smooth, defect-free, and morphologically uniform films throughout the entire coated area [24, 25]. In the case of meniscus-guided techniques, this means controlling many interdependent parameters to ensure smooth, defect-free, and morphologically uniform films [26]. A key part of this process relates to ensuring the rheological properties of the ink and surface tension tuning to ensure uniform wetting of the meniscus, and to prevent solid-phase segregation and sedimentation [27, 28]. The next key part relates to drying, where solvent evaporation must also be controlled in such a way as to maintain control of capillary flows and Marangoni flows, thereby limiting effects such as coffee-rings and uneven nucleation [29]. In coating techniques that involve some type of drying, controlling what happens when the solvent dries are at least as important as the deposition technique itself. The drying kinetics must also be controlled in such a way to limit the trapping of defects, that may also state non-equilibrium states; rapid drying kinetics can trap defects, slowly drying allows the formation of pinholes and voids due to excess solvent [30, 31]. When drying time is not controlled, spontaneous and uncontrolled crystal growth will typically occur [32]. To limit film structure gradients in grain size, homogeneous nucleation and crystal growth must be achieved throughout the film. More problems can occur due to varying substrate surface energy and contact line pinning leading to ridges and edge artifacts [33]. These microscopic defects can be shown by the disparities in film thickness and poor uniformity, often the byproduct of solid-phase segregation during the printing or drying events [18]. Coating parameters such as coating speed, head–substrate distance, and web tension must be controlled to get best results for minimal thickness variations for the film [34]. In this regard, real-time measurements of film thickness during the printing process such as roll-to-roll (R2R) will allow for in-line optimization of operational parameters to reduce thickness variation and maximize uniformity [35–37]. Recent advances have highlighted R2R coating not only as a scalable deposition method, but also as a transformative platform for high-throughput, continuous, and cost-effective manufacturing of perovskite modules under ambient conditions [38], where the implementation of such real-time thickness monitoring is essential to rigorously manage coating dynamics, drying behavior, and quality control. The way to address these issues starts with developing methods to evaluate the uniformity of perovskite films with high spatial resolution across the entire substrate. This is important for the scalable production of high-quality films.

In literature, spatial mapping has been used to study a number of film and device properties using spatially resolved methods, including photoluminescence mapping, light-beam-induced current (LBIC), Raman and Fourier Transform Spectroscopy (FTIR), micro-X-ray Diffraction (XRD), Scanning Electron Microscopy (SEM) or Atomic Force Microscopy (AFM), and X-ray Photoelectron Spectroscopy (XPS) [20, 39–43]. Each of these techniques has afforded a complete understanding of the different possible variations of film morphology, molecular composition, or structure [44]. Similarly, in fully assembled devices, electroluminescence (EL) and infrared thermography mapping have been used to segment the active area into subcells or regions in order to assess local efficiency, identify hotspots, and detect underperforming zones, providing a comprehensive evaluation of film uniformity and device performance [45]. Although these techniques work well, most of them are destructive and can include cutting samples, layer separation, or doing other evaluations from post-deposition, like measure in subcells the final PCE [46, 47]. Therefore, if you are trying to make any type of real-time feedback with an industry-relevant quality control process, these are relatively incomplete techniques because they are not real-time and are unsuitable for scalable production environments. In particular, continuous production scenarios, and especially R2R printing processes, require rapid, continuous, and non-destructive evaluations for quality control and quality assurance of the film as a function of the consistency of device performance.

To address this need, recent research has examined the application of machine learning (ML) and deep learning (DL) techniques for in situ inspection of various photovoltaic technologies. Ultimately, the use of experimental datasets and AI-based models has allowed researchers to propose automated systems that have the ability to predict important characteristics of solar cell components and modules, while observing the production process without breaking. In terms of silicon-based photovoltaics, a team led by Singh et al. created a machine vision system for classifying macro-defects (i.e., cracks, inactive areas, contaminants, and defective interconnects) using EL images and providing feedback to the production line in real-time [48]. In the same respect, Kropp et al. offered a quantitative way to predict power loss in polycrystalline silicon modules with over 95% accuracy from pairs of EL images [49]. Deitsch et al. trained a convolutional neural network (CNN) on over 2000 EL images to identify defective cells, and their trained model correctly identified visible cracks, hot spots, and faulty contacts with 88% accuracy [50]. In the context of printed organic solar cells, a R2R inspection system which combined printed photovoltaic and geometric location parameters along with printing processes was created by Wei et al. They recognized relevant features with sequential design of experiments using ML models [51]. These were then optimized to establish process parameters, which reduced development time. In addition to being applied in the compositional design phase in perovskite-based systems, ML is being incorporated in an increasing number of processes, including optoelectronic property prediction, degradation monitoring, and detection at both micro- and macro-scales. Taherimakhsousi et al. used a modified VGG16-based CNN to predict film thickness and current density from transmission images and profilometry data [52]. They also trained a second model to quantify defects in spin-coated and slot-die-coated films, correlating predictions with the performance of 25 cm^2 minimodules using a dataset of 612 images. Harth et al. proposed a rapid characterization technique that combines spectral measurements with machine vision to extract optoelectronic properties of perovskite thin films in real time [53]. More recently, Laufer et al. demonstrated a DL strategy to enhance the in-situ metrology during large-scale perovskite film fabrication [54]. Their framework incorporated real-time monitoring of precursor composition, prediction of final device efficiency prior to assembly, and the generation of process control recommendations by forecasting real-time signals and their impact on performance.

Although significant advances have been made, many of these efforts try to predict the overall efficiency of the device based on the optical characteristics of only one or two isolated layers. Ultimately, the performance as the end result depends on the interaction and uniformity of most typically five functional layers, all contributing to the final performance through various and complex physical and chemical interdependencies. As a result, these strategies are not yet scalable or fully integrable as early-stage inspection tools within multilayer fabrication processes. A more practical and scalable approach is to begin with the inspection of the perovskite layer itself, the most critical and sensitive component, by establishing thickness as a primary quantitative indicator of film uniformity. Given the strong correlation between film thickness and perceived color in thin perovskite layers, optical imaging offers a powerful, non-destructive pathway for inferring thickness variations across large areas. Utilizing this relationship enables early-stage quality control prior to the full assembly of devices and establishes considerations for incorporating this in continuous production environments.

A major difficulty in building a regression model relating to film color and thickness is minimizing the noise of the scattered light that will be experienced during reflected-light imaging of certain perovskite morphologies. In recognition of these differences in film morphology, we developed a custom inspection prototype that relied on the far more uniform and reproducible lamp emission profile found in transmitted-light illumination and therefore ensured that image acquisition was performed in a uniform and consistently illuminated region for the entire film surface, thus reducing optical artifacts and providing a well-controlled basis for image-based thickness analysis.

With this information, we developed an ML framework that predicted perovskite film thickness directly from red-green-blue images with very high spatial resolution. The results confirmed the precision and general applicability of the method across two perovskite compositions (and other functions such as color) regardless of thickness, with root-mean-square error (RMSE) below 26 nm. By demonstrating a relationship with PCE and EL across a 25 cm^2 set of minimodules, we showed that there are opportunities that would allow for fast, quantitative, and non-destructive quality control. The approach is seamlessly integrated into continuous production lines and is well suited for monitoring film homogeneity during fabrication. Implemented within an R2R workflow, the system allows in situ estimation of spatial thickness variations after annealing, including quantification of the median absolute deviation (MAD) in both the X and Y directions. This allows for the identification of directional inhomogeneities, defects that would exist in a pattern over large spatial scales that address major limitations of newer inspection modalities, and real-time process optimization. Figure 1 summarizes the complete inspection prototype, the method developed to execute it, and the approach of doing better non-destructive quality controls on PSC manufacturing that have been described in this work.

2 | Results and Discussion

2.1 | Validation of Model Performance

To assess generalization across the entire dataset, a 5-fold cross-validation was performed using the KFold function. Each model was trained for 30 epochs per fold. The performance across folds is reported in Table 1, which shows the minimum validation mean squared error (MSE achieved and the epoch at which it occurred.

The evolution of training and validation MSE values during the 30 epochs for both compositions is shown in Figure 2a,b. As seen in the plots, the MSE drops significantly within the first 5 epochs and stabilizes thereafter, indicating rapid convergence. The small gap between training and validation MSE suggests minimal overfitting and good generalization.

For the $MAPbI_3$ model, the average validation MSE across folds was $\approx(5.50 \pm 1.40) \times 10^{-4}$, while the $FAPbI_3$ model achieved an average of $\approx(8.70 \pm 2.80) \times 10^{-4}$. In both cases, the model weights from the fold with the lowest validation MSE were selected for final deployment.

As previously mentioned, samples were set aside for model evaluation. Figure 2c,d displays the comparison between the actual thicknesses and the predicted values, along with the error (residuals, orange symbols) from the models with the best weights from the cross-validation (fold 1 for $MAPbI_3$ and fold 2 for $FAPbI_3$). When the corresponding images were passed through the trained model, the predicted thickness values were obtained. Comparing only the predictions with the actual thicknesses measured by profilometry yields the plot in Figure S1a. Ideally, all points should lie on the line $y = x$; however, some exhibit slight deviations. Examining the sample-by-sample behavior (Figure 2c), the largest errors concentrate around 500 nm, though they remain below 60 nm (orange points and line). In this set, the model achieved an R^2 of 0.985 and an RMSE of 18 nm.

In Figure S1b, errors are shown as the absolute values of the residuals $(r_i = y_i - \hat{y}_i)$, i.e., the differences between the true values (y_i) and the predicted values $(\hat{y}_i)$. Each point indicates how much the prediction deviates from the true thickness. Notably, errors tend to increase at higher thickness: around 500 nm they reach 40–60 nm, whereas below 300 nm they rarely exceed 20 nm. This suggests that the model is less precise at high thickness and that errors are not uniform across the range. This result indicates that the model requires improved generalization in that thickness range to optimize training and overall performance.

However, it is important to consider the labeling method for the training dataset. Labels were generated by a semi-automated method, allowing rapid thickness assignment, but the images did not exactly match the profilometry scan areas. As a result, a non-typical profilometry reading might have been paired with a representative image, or a non-representative image might have been paired with a correct profilometry reading. This less precise labeling can influence model evaluation, and its effect was most pronounced at higher thicknesses. However, it provides a fast-paced approach for assembling the dataset and incorporating new perovskite compositions.

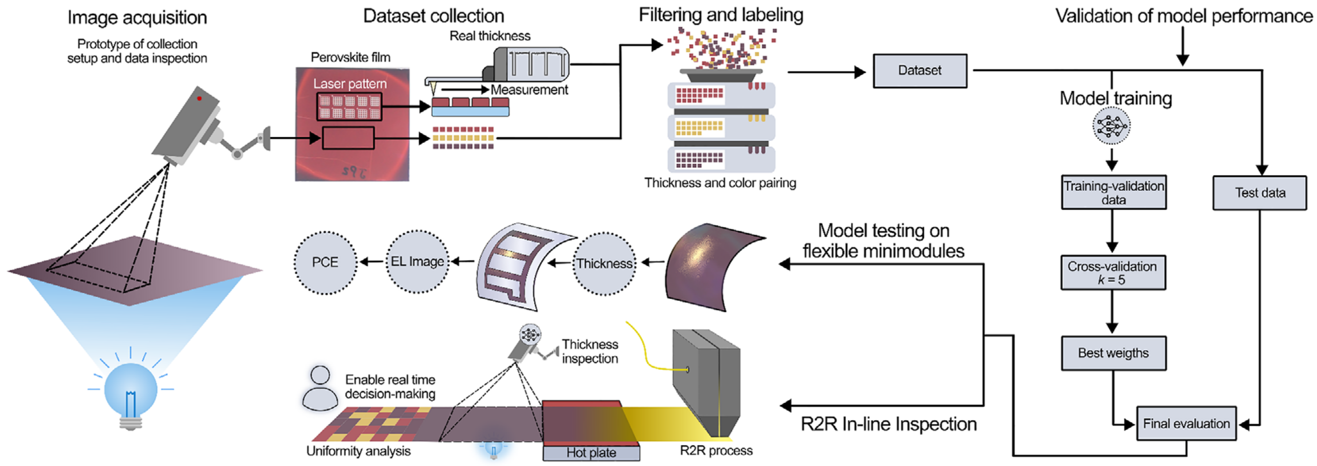

FIGURE 1 | Process schematic for the development of the machine-vision-based profilometer, showing the stages of data collection, data filtering, model training, testing and demonstration on real flexible perovskite mini-modules; and in-line validation of the system.

TABLE 1 | Model performance during 5-fold cross-validation for the perovskite models $MAPbI_3$ and $FAPbI_3$.

Fold	Optimal Epoch ($MAPbI_3$)	Min Val MSE ($MAPbI_3$)	Optimal Epoch ($FAPbI_3$)	Min Val MSE ($FAPbI_3$)
Fold 1	28	3.90×10^{-4}	24	1.27×10^{-3}
Fold 2	26	4.68×10^{-4}	28	6.14×10^{-4}
Fold 3	30	5.81×10^{-4}	30	1.03×10^{-3}
Fold 4	22	5.64×10^{-4}	24	7.87×10^{-4}
Fold 5	28	7.50×10^{-4}	25	6.27×10^{-4}
Average ± Std. Dev.	—	$(5.50 \pm 1.40) \times 10^{-4}$	—	$(8.70 \pm 2.80) \times 10^{-4}$

Applying the same evaluation procedure for the $FAPbI_3$ composition using isolated images yielded predicted thickness values. Comparing these predictions with the actual profilometry measurements resulted in the plot shown in Figure S2a. As with $MAPbI_3$, the deviation from $y = x$ was minimal, and predictions closely approximated the actual values. A sample-by-sample inspection in Figure 2d highlights potential labeling errors in the ≈200 and ≈600 nm ranges, where outlier measured points stand out from the trend line. Residual analysis of the isolated set (Figure S2b) shows errors ranging from 0 to 60 nm and, in atypical cases, exceeding 80 nm. The highest variance occurs at greater thicknesses, which may explain the lower precision in that range. The corresponding predicted value remains on the trend line, indicating that the image retains the characteristic features of the other data in that range and that the model generalizes properly. Predictions near 400 nm deviate more widely from the trend line. This result may be due to less precise generalization in that specific thickness range. In this set, the model achieved an R^2 of 0.986 and an RMSE of 25 nm.

The metrological traceability of the machine-vision based tool is established through the measurements obtained by the stylus profilometer (KLA Tencor D600 and Bruker Dektak) and the final results are reflected through the isolated test set, where multiple samples that were outside the training process were tested (692 samples for $MAPbI_3$ and 489 for $FAPbI_3$). The intrinsic uncertainty of the method arises from two primary sources: the baseline measurement error of the profilometer and the convergence error of the CNN during the training phase. The predictive accuracy and repeatability of the system were further validated using an independent validation set of isolated samples ($N = 692$ for $MAPbI_3$; $N = 489$ for $FAPbI_3$). The resulting overall measurement uncertainty is represented above by the RMSE values as aforementioned (of 18 nm for $MAPbI_3$ and 25 nm for $FAPbI_3$) representing the high precision of the mathematical fit to the training data. Despite variability observed in both models across each perovskite composition, most errors remain below 20 nm. The highest variance occurs at greater thicknesses, which may explain the lower precision in that range. The fundamental working principle of the proposed machine-vision method relies on the relationship between film thickness and the attenuation of transmitted light. When maintaining a constant incident light source (Figure S3) and sensor calibration, the variation in the recorded RGB intensity is primarily driven by the absorption characteristics of the perovskite layer. According to the Beer-Lambert Law, the intensity of transmitted light through each color channel (Red, Green, and Blue) serves as a proxy for the optical path length within the material. Given that perovskite exhibits strong and thickness-dependent absorption across the visible spectrum, these RGB values provide a distinctive signature for thickness estimation. However, an idealized analytical approach often fails to account for the secondary optical phenomena inherent in scalable manufacturing, such as thin-film interference and moderate surface roughness-induced scattering. The

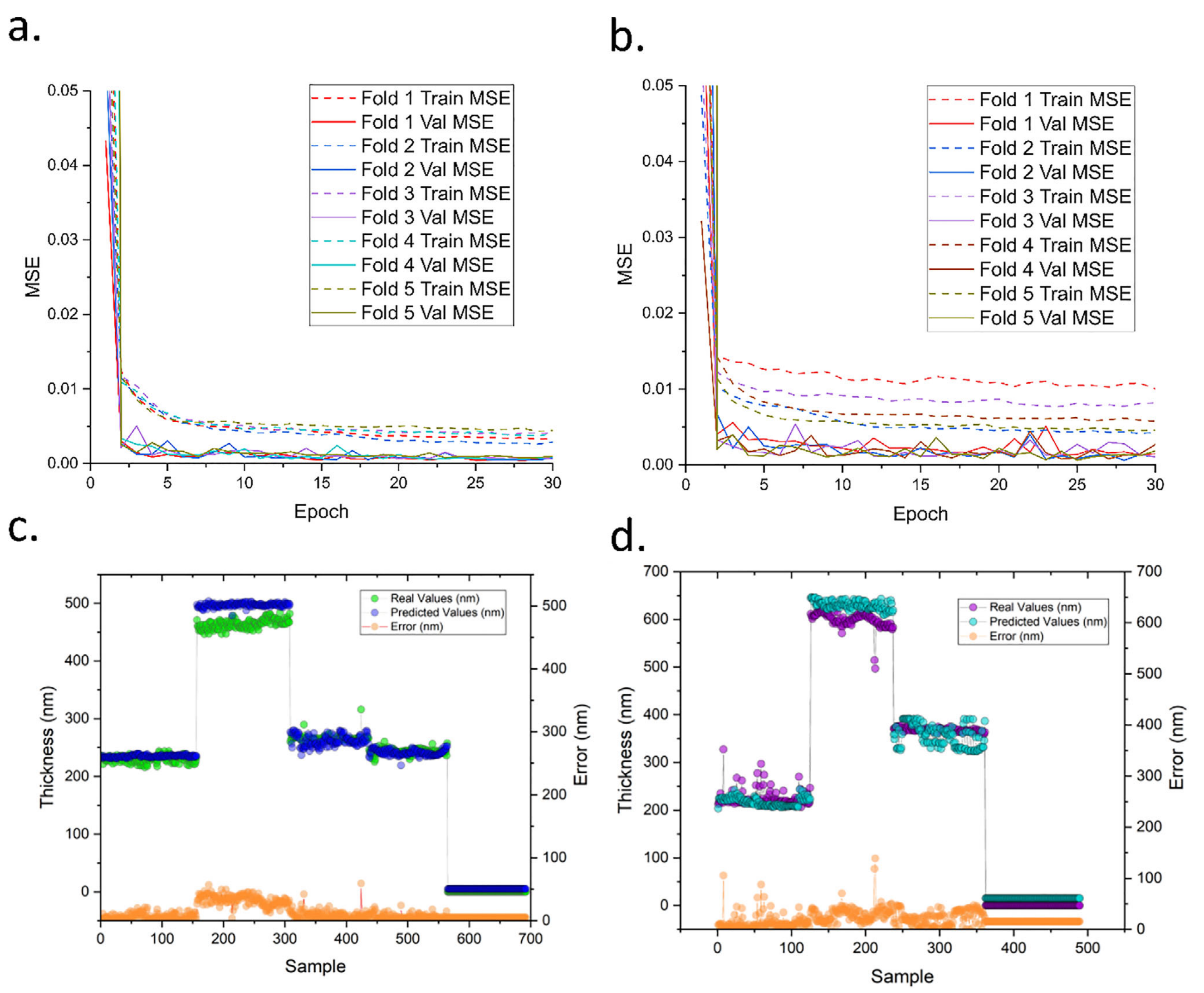

FIGURE 2 | Evolution of training and validation MSE over 30 epochs of cross-validation for the perovskite model: (a) $MAPbI_3$ and (b) $FAPbI_3$. Performance of the thickness measurement model on the isolated test set where (c) shows the actual versus predicted thickness for $MAPbI_3$ with residuals, and (d) actual versus predicted thickness for $FAPbI_3$ with residuals.

implementation of a data-driven CNN is therefore essential to transcend simple empirical parameter fitting. By extracting high-dimensional spatial and spectral features from the RGB matrices, the model accounts for these complex optical relationships that a univariate model would ignore. This "learned" robustness ensures the mapping between the optical signal and thickness remains reliable even when the film deviates from an ideal plane-parallel absorber, providing a highly reproducible metrology tool for in-line monitoring of flexible optoelectronic devices. Moreover, while the model is sensitive to secondary optical effects such as scattering from microstructure defects or material degradation, these factors were controlled during the experimental phase to ensure that color variations were predominantly associated with thickness. Consequently, by standardizing lighting conditions and using non-degraded films, the system functions as a robust, reproducible metrology tool for real-time monitoring in scalable manufacturing environments. While this setup relies on standardized data collection parameters, the methods, algorithms, and neural network architectures provided herein deliver a robust framework to replicate this metrology instrument. Overall, the performance of the system is remarkable for a prototype designed to function equivalently to an in-line optical profilometer using only a webcam.

2.2 | Model Testing on Flexible Minimodules

Flexible solar mini-modules were fabricated as described in the Materials and Methods section. To validate the model's robustness across multilayer architectures, Figure S4 compares the UV–Visible absorption spectra of the various substrates (Glass/Indium Tin Oxide (ITO)/NiO_x and Polyethylene Terephthalate (PET)/ITO) with the absorption profiles of the $MAPbI_3$ and $FAPbI_3$ films. These results confirm that the optical contribution of the underlying transport layers and substrates within the visible spectrum is negligible on a macroscopic scale relative to the dominant absorption of the perovskite layer. While a minor increase in substrate absorption is observed toward the near-infrared region, the emission spectrum of the 9000K LED source (Figure S3) exhibits low intensity in this band, effectively decoupling substrate variations from the thickness estimation. These observations underscore that the RGB-to-thickness correlation is primarily driven by the photoactive layer, facilitating accurate in-line monitoring during intermediate fabrication stages before full device completion. Images of the active areas were processed through the system to provide thickness measurements across the entire surface. The devices were fabricated in two batches using the same processing parameters, and the resulting thicknesses are shown in Figure S5. The labels on each boxplot represent the average thickness recorded for each mini-module. Even with the same fabrication parameters, samples from batch 1 (samples 1–6) exhibited slightly lower thicknesses than those from batch 2 (samples 7–12). Similarly, some samples present a greater number of outlier values, which correspond to thickness measurements that deviate significantly from the rest of the predicted thickness data. This fact could be due to defects, as seen in samples 2, 3, and 6. Samples 6–12 also show greater thickness variability, reflected by larger box sizes and indicating higher surface roughness. The thickness differences between the two batches may be the result of slight variations in the local environment during processing or in the ink concentration of solids.

The coefficient of variation (CV) of the predicted thickness data is defined as the standard deviation (σ) divided by the mean ($\bar{x}$). With these values, sample 2 exhibits the highest CV among all samples. Furthermore, except for sample 2, samples 6–12 have higher CVs than samples 1–5. The results and J-V plots for the CVs of the thickness and the measured photovoltaic parameters of the completed devices are presented in Table S1 and Figure S6.

Figure 3 presents a global comparison of the two batches of mini-modules, each with a different average thickness as previously mentioned, relating device efficiency and the CV of the thickness. Additionally, the electroluminescence results of the extreme points are shown. Remarkably, mini-modules 1–6 (red dots) exhibit greater dispersion in CV values (Figures S7–S13). Here, it becomes clear that these results indicate that within this first group, device performance is influenced by thickness uniformity and defects in the perovskite layer. The highest efficiency was achieved by mini-module 5 (lowest CV, top left Figure 3), whereas the lowest efficiency was observed for mini-module 2 (highest CV, bottom right Figure 3).

Upon analyzing the captured images derived from the perovskite film of mini-module 2, it is apparent that the third active area contains a significant defect where the perovskite film is missing (bottom right, Figure 3). Consequently, in the thickness map the model assigns zero thickness to this region. A smaller defect is also detected in active area two, which is clearly visible in both the original images and the thickness map. The camera remained fixed in a constant position, so one pixel corresponds to approximately 0.057 mm in width. The model processes sections of 5×5 pixels (equivalent to an area of 0.081 mm^2) at a mean speed of 32 ms, providing a single predicted value per block. Thus, each 5×5-pixel block is represented as a single pixel in the thickness map, resulting in a dimensionally reduced image.

This process suggests that if a defect is visible in the thickness map and is assumed to be circular, its diameter is equal to or greater than 321 μm. While this spatial averaging improves robustness to local noise, it reduces the resolution of the final thickness map and may obscure narrow or localized defects, however, the dimensions of processed sections could be reduced at the expense of increased processing time. The absence of the perovskite film highlights the defective region with a lack of luminescent activity as shown in the corresponding electroluminescence image. Additionally, the visible defect at the bottom of active area 2 also reveals a region of reduced activity. Furthermore, in the electroluminescence images, line-shaped defects exhibiting reduced light intensity are noticeable throughout the active areas, likely related to marks on the transparent conductive oxide (TCO), in this particular case the ITO, resulting from handling or cleaning procedures.

When observing a perovskite film with greater uniformity (i.e., a lower CV), such as that of mini-module 5 (top left, Figure 3), the corresponding electroluminescence image presents defects that do not correlate with those visible in the thickness mapping. Therefore, those defects can be attributed to other layers, either preceding or succeeding the perovskite layer. Additionally, active area 1 shows higher luminescence intensity compared to areas 2 and 3, which may be due to slight differences in their dimensions: area 1 is approximately 151 mm^2, whereas areas 2 and 3 are 165 mm^2 each. In several of the electroluminescence images (Figures S7b–S18b), this effect is evident, with the first cell of each mini-module exhibiting higher luminescent intensity than the others.

In contrast, the second group of mini-modules (blue dots), which has a slightly higher average thickness (as previously shown), exhibited CVs ranging from 4.26%–5.36%, reflecting less dispersion compared to the first group (Figures S13–S18). This group included mini-module 10 with the highest efficiency (PCE = 6.24%, top right Figure 3), and mini-module 12 (PCE = 3.5%, bottom left Figure 3) with the lowest efficiency. Within this group, the performance peak may have been influenced by the slight increase in thickness. However, the variation in efficiency among devices suggests defects in layers besides the perovskite or undetected morphological abnormalities as additional limiting factors, as evidenced in the electroluminescence images of mini-modules 8 (Figure S14) and 12 (bottom left Figure 3), which are the lowest-performing within the second group. In these images, defects not attributable to the perovskite layer are evident, manifesting as dark areas in the active regions.

Examining the thickness distribution for each active area of the first batch of mini-modules enables assessment of the model's performance against device results. Figure S19a presents the boxplots for each active area of mini-module 2. Although the average thickness is relatively uniform among the three areas, significant outliers are observed. In particular, active area 1 shows values exceeding the average thickness by up to 100 nm, while in active area 3, minimum thickness values close to zero are recorded. Figure S19b shows the thicknesses for mini-module 5, which demonstrates greater uniformity than mini-module 2. In this case, outliers do not exceed 50 nm above the average thickness. Although a slight variation in thickness between active areas is detected, this difference falls approximately within the uncertainty range of the model developed for $MAPbI_3$ perovskite,

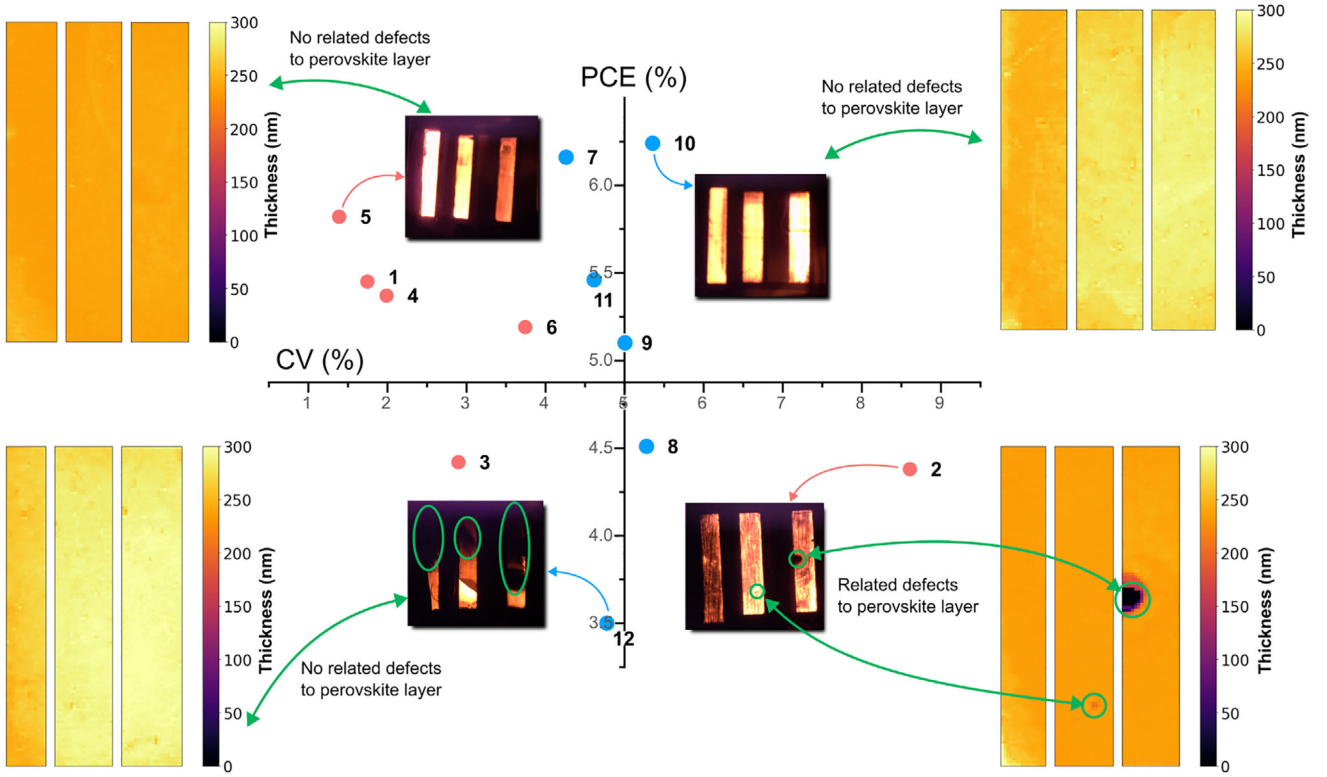

FIGURE 3 | Overall comparison of the CV of perovskite layer thickness versus PCE of the fabricated mini-modules, along with electroluminescence images and thickness maps for the highest and lowest performing devices.

which, as mentioned earlier, has a RMSE of 18 nm on the isolated test set.

While control over the uniformity of the perovskite layer is necessary to achieve good device performance, the complexity of the device (associated with the presence of multiple layers in addition to the perovskite) means that achieving a uniform perovskite layer is not a sufficient condition to reach a final high performance. To address this, future work should extend the inspection framework to additional layers by incorporating alternative imaging strategies other than visible imaging (for instance, UV-imaging for high bandgap materials), enabling layer-by-layer assessment of the print, and thereby moving closer to fully automated, high-throughput fabrication of large-area perovskite solar modules.

Nevertheless, in a continuous roll-to-roll manufacturing environment, the ability to rapidly evaluate perovskite-layer quality and uniformity in real time remains a high-value capability, providing opportunities to develop in-line inspection strategies through the analysis of high-spatial-resolution thickness data.

2.3 | R2R In-Line Inspection

In high-throughput printing systems, machine-vision tools monitor the printed layer in real or near-real time. Such monitoring facilitates parameter adjustments, shifting reliance from operator experience to statistical analysis of layer uniformity and defect incidence based on the current settings. Figure 4a is the result of the in-line scanning process of a $MAPbI_3$ perovskite layer from the developed program for this task, that uses the same model from the static mapping implementation, but predicting the values in real time as Supporting Information S1 shows. The scanning was performed over a 4.8×21 cm printed film with a web speed of 0.3 m min^{-1} as mentioned before.

Some regions within the coating boundaries appear in the results as uncoated or with a thickness equal to zero. These areas are being misinterpreted by the model due to the high roughness and porosity of the film. Even though the measurement occurs in a controlled environment designed to limit reflected light, some illumination can still reflect off the prototype walls and onto the film. In highly porous regions, this incident light results in increased scattering due to elevated roughness, causing the film to reflect white light, leading the model to inaccurately interpret these areas as having zero thickness. This phenomenon has been documented in various studies where perovskite films images have been taken and is a characteristic morphology found in regions subject to rapid solvent extraction during the film formation process for printed layers [52, 55–58]. The operational boundary of this machine-vision approach is fundamentally governed by the interplay between film surface morphology and the optical configuration. Mechanistically, the model maintains a degree of tolerance toward moderate scattering through the 5 × 5 pixel block processing, which effectively functions as a spatial low-pass filter for high-frequency noise related to surface texture. However, the transition to macroscopic roughness (typically exceeding 100 nm) and extreme porosity triggers a regime where diffuse scattering dominates over coherent transmission. As evidenced in Figure 4, regions with nominal roughness (~20–30 nm) exhibit stable and distinguishable color-thickness vectors,

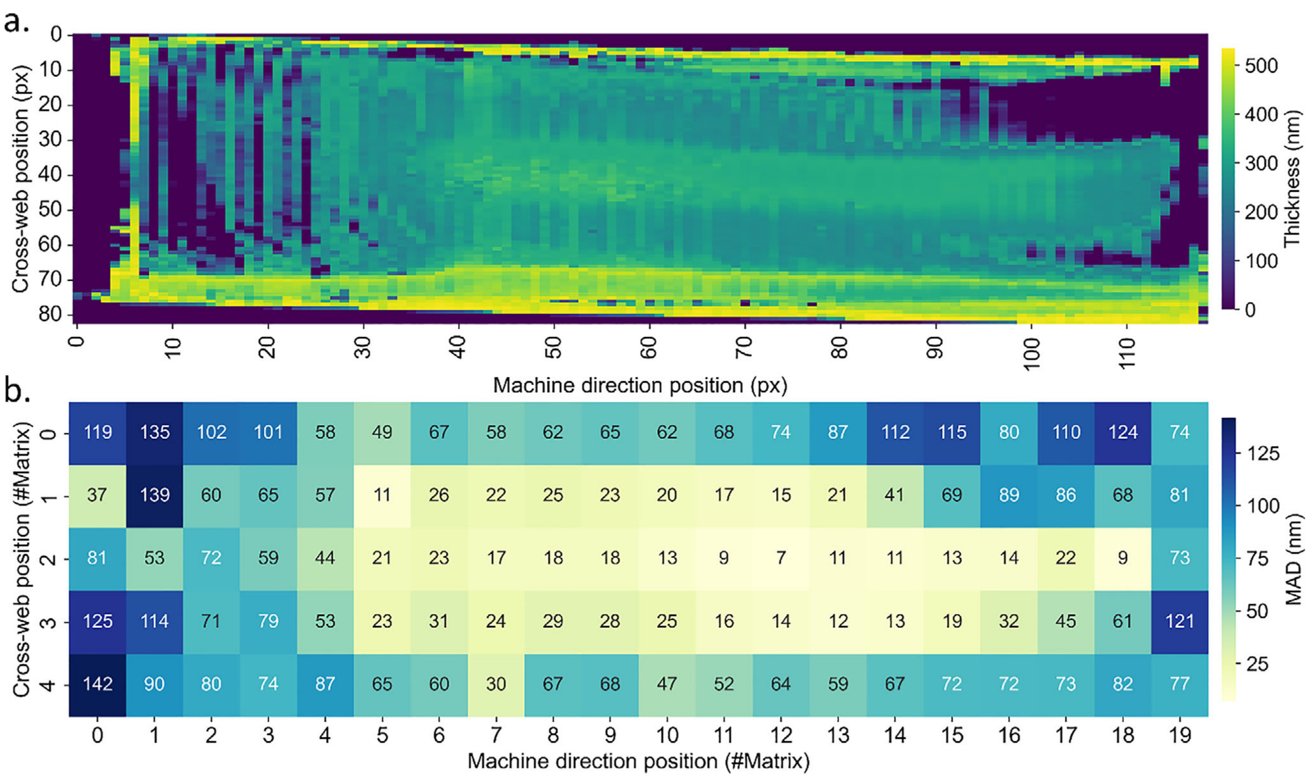

Cross-web position (#Matrix) \ Machine direction position (#Matrix)	0	1	2	3	4	5	6	7	8	9	10	11	12	13	14	15	16	17	18	19
0	119	135	102	101	58	49	67	58	62	65	62	68	74	87	112	115	80	110	124	74
1	37	139	60	65	57	11	26	22	25	23	20	17	15	21	41	69	89	86	68	81
2	81	53	72	59	44	21	23	17	18	18	13	9	7	11	11	13	14	22	9	73
3	125	114	71	79	53	23	31	24	29	28	25	16	14	12	13	19	32	45	61	121
4	142	90	80	74	87	65	60	30	67	68	47	52	64	59	67	72	72	73	82	77

FIGURE 4 | Log of data collected during the in-line scan of the $MAPbI_3$ perovskite film, where (a) shows the raw thickness measurements of the entire film and (b) shows the MAD computed over 5 × 5 pixel sectors.

whereas regions with roughness surpassing the 100 nm threshold (often associated with poor device performance) generate significant scattering artifacts. Figure S20a–d shows an image of a $MAPbI_3$ film along with its respective roughness measurements, representing the measurement limits of this specific setup under the current system training. While these artifacts currently limit thickness estimation in highly porous zones, they also serve as an implicit quality indicator for non-optimal film morphologies, a feature that could be refined by incorporating alternative illumination geometries or targeted training on high-porosity datasets. This issue could be addressed by training the model with additional images explicitly labeled as high-porosity regions or by improving the device enclosure to further reduce internal reflections.

Having the actual thickness values for the entire printed area allows the use of statistical metrics to characterize specific regions of the layer. Figure 4b shows the MAD, defined as $\text{MAD} = \text{median}(|x_i - \text{median}(X)|)$. This statistic minimizes the influence of outliers hence, the MAD value for each sector indicates (in nanometers) the deviation from the population median while down-weighting any outliers. The most uniform sector of the printed layer spans machine-direction positions 5–13 and cross-web positions 1–3, with MAD values ranging from 7 to 29 nm. Figure S21a shows the mean thickness in these sectors, ranging from 342 to 365 nm.

Similarly, the CV on Figure S21b exhibits comparable behavior expressed as a percentage. Additionally, a $FAPbI_3$ perovskite film was coated under the same conditions and length, and analyzed using the model specifically developed for this composition. The corresponding scanning images and statistical metrics are provided in Figures S22 and S23. As with the previous composition, sectors exhibiting better uniformity (i.e., lower MAD and CV values) can be identified within the initial printed regions of the film (machine-direction positions 0–5 and cross-web positions 0–4). These figures also display the mean thickness for each corresponding sector, along with similar scattering-light effects. Beyond the data presented here for these two printed films with different compositions, this approach demonstrates its potential not only to identify the most uniform sectors but also to provide timely feedback on the ongoing printing process. Such real-time insights enable informed, in situ parameter adjustments, ultimately leading to improved reproducibility and the fabrication of films that yield large-scale devices with homogeneous performance.

For future work, the processed in-line metrics collected by this method are ready to be integrated into a closed-loop control system that could monitor CV and MAD values and adjust printing parameters, such as pumping rate, printing speed, or gas-knife conditions, bringing perovskite photovoltaics closer to smart manufacturing.

3 | Conclusions

In this work, a versatile in-line inspection prototype for printed perovskite films on flexible substrates was designed, built, and validated. By combining a low-cost webcam-based optical setup with a deep-learning regression model, we demonstrated thickness estimation with coefficients of determination of 0.985 (R^2)

for $MAPbI_3$ and 0.986 for $FAPbI_3$, and root-mean-square errors of 18 and 25 nm, respectively. These results confirm that a simple transmitted-light imaging setup can achieve precision comparable to that of conventional profilometry instruments in a non-destructive approach. When this prototype was used on 25 cm^2 solar mini-modules, an inverse correlation was observed between thickness variability (quantified by the CV) and PCE, suggesting that greater layer uniformity enhances device performance.

This methodology was extended to a R2R coating line, performing real-time thickness scans over a 4.8 × 21 cm printed film. In addition, MAD values by sector were computed to identify the most uniform regions. This capability enables immediate, data-driven adjustments to coating parameters, thus shifting process control from operator intuition to quantitative feedback.

Certain challenges remain related to highly porous or rough regions that can scatter light in ways that mimic zero-thickness areas. However, this issue can be addressed by augmenting the training dataset with labeled high-porosity images and enhancing the enclosure to suppress reflections. Also, while perovskite thickness uniformity is a necessary condition for optimal device performance, it is not sufficient (multilayer interactions and defects in subsequent layers also have a significant influence) and highlights the need to inspect quality layer by layer rather than treating the entire system as a single unit. Future work should therefore focus on extending in-line inspection to other stages of the manufacturing process, additional film layers (e.g., charge-transport and encapsulation layers) and integrating spectral or fluorescence imaging to capture compositional and morphological defects beyond thickness. Moreover, while a webcam-based system is clever and cost-effective, it is limited in spectral resolution, and there is an opportunity to improve the sensitivity range for detecting super-thin or transparent layers.

4 | Experimental Methods

As previously mentioned, to develop a regression model capable of relating the color of perovskite films to their thickness, a prototype was designed and fabricated to capture the perovskite film images using transmitted light (Figure S24). This illumination arrangement was chosen to reduce noise produced by light scattering in reflective-based illumination setups for certain perovskite-layer morphologies, as evidenced in images from other studies [50, 53, 59]. The setup comprises two light-tight enclosures: One housing the camera and fixing it at a predetermined height and position, and the other containing the lamp and a diffusing screen. Images were captured with a Logitech C920 camera at a resolution of 1920 × 1080 pixels and a 24-bit color depth.

The prototype's dimensions were adjusted to fit the available space of the Smart Coater system provided by Coatema at Swansea University. This configuration allows both data collection and inspection during the printing process by placing the device immediately after the annealing oven. In total, two prototypes were fabricated: one for the SPECIFIC group at Swansea (UK) and one for the CIDEMAT group at the University of Antioquia (Colombia).

4.1 | Data Collection for Model Training

Prior to image captures for the dataset, ITO-coated glass substrates were prepared following a standardized cleaning and activation protocol. Substrates were sequentially sonicated in deionized water, acetone, and isopropanol, then UV-ozone treated for 10 min to enhance surface wettability. Perovskite precursor solutions ($MAPbI_3$ in acetonitrile (ACN)/methylamine with Methylammonium chloride (MACl), and $FAPbI_3$ in 1,3-Dimethyl-2-imidazolidinone (DMI), ACN, 2-Methoxyethanol (2-ME), and MACl) were deposited by spin-coating at varied spin speeds to achieve a range of thicknesses; for thinner films, the concentration of the perovskite precursor solution was reduced, and spin parameters were adjusted as detailed in Tables S2 and S3. Following deposition, films were annealed at 100°C for 10 min for $MAPbI_3$ and 150°C for 10 min for $FAPbI_3$, then subjected to laser scribing before image capture. Prior to $FAPbI_3$ depositions, substrates were coated with NiO_x and Self-assembled monolayers (SAM)-Me-4PACz to improve wettability. The complete coating parameters and ink formulations can be found in Note S1.

A laser-scribing pattern was applied to define a grid of 4 × 4 square sectors (Figure S25), thus enabling thickness measurements with four-region sweeps (Figure S26), acquiring 160 measurements per sample. Thickness measurements were performed using a KLA Tencor D600 profilometer at Swansea University and a Bruker Dektak profilometer at the University of Antioquia. Both instruments scanned the scribed sectors to extract film thickness. Scan data were processed with custom Python scripts to detect and discard outliers (due to dust or scribing-related debris). The resulting thickness values were recorded in a structured annotation file linking each sector to its mean thickness. The full thickness data gathered per sample are shown in Figure S27.

Image acquisition was performed after laser scribing. The sample was placed at a fixed position inside the camera enclosure. Lamp-to-sample and camera-to-sample distances were fixed throughout the image capture process. A collage of the images obtained from the SPECIFIC group data is shown in Figure S28. Background images of blank substrates were acquired to capture camera noise and uncovered sectors for model training.

Finally, the structured dataset comprises, for each sector, the transmission image captured under controlled illumination (with fixed camera and lamp positions) and the corresponding profilometric thickness measurement. All capture parameters (camera model, resolution, bit depth, illumination settings), distances, and processing scripts were version-controlled and documented to ensure reproducibility. Both datasets with structured data are shared in this work.

4.2 | Training of the Model

To evaluate the thickness prediction performance of the proposed architecture, we trained and validated models on two perovskite compositions: $MAPbI_3$ and $FAPbI_3$. Both models were trained

TABLE 2 | Data Augmentation and Split for Training, Validation, and Testing.

Source	Training set		Validation set	Testing set
	Raw data	**Augmented data**		
SPECIFIC $MAPbI_3$	723	10000	181	308
CIDEMAT $MAPbI_3$	906	10000	226	384
CIDEMAT $FAPbI_3$	962	10000	241	489

under identical conditions using a CNN architecture named as HDUnet [60, 61], which integrates components from UNet, DenseNet, and HRNet. UNet it used for its effectiveness in spatial feature extraction [62], DenseNet for its ability to promote feature reuse and efficient gradient propagation [63], and HRNet for its ability to maintain high-resolution representations while exchanging information across multiple scales [64].

4.2.1 | Training Configuration

The training process employed the AdamW optimizer with an initial learning rate of 0.001 and a weight decay of 0.1 per epoch. The learning rate was progressively reduced using a decay schedule described by Equation (1), where the learning rate (lr) is updated at each epoch n as:

$$Ir = Ir \times 0.995^{(n+1)} \tag{1}$$

The MSE was used as the loss function to evaluate model performance. This metric, commonly used in regression tasks, measures the average squared difference between the predicted and actual thickness values. Both the training and validation MSE were monitored during the 30 training epochs to evaluate overfitting and convergence. Training was conducted using a GPU with 15 GB of RAM available in the Google Colab environment.

4.2.2 | Data Preparation

Table 2 summarizes the data distribution used for training, validation, and testing. For the $MAPbI_3$ composition, image data collected from both SPECIFIC and CIDEMAT laboratories were combined to strengthen the generalization capacity of the model. Despite potential minor variations in illumination and imaging equipment, both datasets were obtained under equivalent lighting conditions using the same prototype system.

To ensure unbiased model evaluation, some samples were withheld entirely from training and reserved for testing and validation. Those samples were 7, 8, 5, and 6 for $MAPbI_3$, and samples 3, 6, and 11 for $FAPbI_3$ (Figure S27). Additionally, zero-thickness data points images were included to help the model recognize regions not covered by the perovskite films.

Data augmentation techniques, including image flipping, salt-and-pepper noise addition, and brightness variation, were applied to expand the training dataset synthetically to 10 000 samples. This approach helps mitigate overfitting and increase the robustness of the model.

4.3 | Minimodule Fabrication and Characterization

For the flexible perovskite minimodules fabrication, a PET/ITO substrate was used (150 ohm/sq). A nickel oxide ink (20 mg/mL in deionized water) was deposited by slot-die coating, following a 10 min UVO treatment of the substrate. A web speed of 1.5 m/min, a gap of 150 µm, and a pump rate of 0.1 mL/min were used. The subsequent layers of the devices were deposited by spin coating as follows. An alumina dispersion diluted using isopropanol (1:20) was deposited at 3000 rpm and 3000 acceleration for 30 s. The $MAPbI_3$ (30% wt.) perovskite was spin-coated at 4000 rpm and 4000 rpm/s acceleration for 30 s, followed by a hot-plate annealing at 100°C for 10 min. The PCBM ink (16 mg/mL in chlorobenzene) was deposited at 2000 rpm and 2000 acceleration for 30 s and annealed at 75°C for 5 min. The Rhodamine (0.5 mg/mL in ethanol) layer was spin-coated at 4000 rpm and 4000 rpm/s acceleration for 30 s. Finally, a 100 nm silver electrode was thermally evaporated. The active area of the devices was 4.5 cm^2.

Based on the training results, twelve $MAPbI_3$ perovskite mini-solar modules were fabricated. These modules incorporated an intermediate imaging step to assess the uniformity and defect density using the regression model. Upon completion, the photovoltaic parameters were measured and electroluminescence images were captured for comparison with the thickness measurements. For the electroluminescence measurement, all imaging was performed under low-light conditions using a custom-made setup consisting of a Nikon D3100 camera set to manual mode, a 720 nm long-pass filter, ISO 3200, a 30-s shutter speed, an f/5.6 aperture, and an applied voltage of 3.5 V (schematic on Figure S29).

4.4 | In-Line Thickness Measurements

For the continuous slot-die deposition experiment an Infinity PV R2R equipment was used (LR2RC750) at CIDEMAT group at the University of Antioquia. A $MAPbI_3$ perovskite ink (20% wt, acetonitrile/methylamine) was slot-die coated over PET/ITO substrates previously cleaned using Isopropanol. No further treatment was done to the substrate. A web speed of 0.3 m/min, a gap of 150 µm using a shim thickness of 150 µm, and a pump rate of 0.3 mL/min were used for the continuous slot-die coating process. A "nitrogen knife" system was placed right after the slot-die head to control the drying process of the films. Once the perovskite films were deposited, annealing was carried out by placing a hot plate set to 100°C beneath the tensioned substrate. The annealing process lasted for 10 min under 30%–40% relative humidity.

$FAPbI_3$ films were coated at a web speed of 0.2 m/min using a 150 µm shim, a 100 µm coating gap, and a pump rate of 0.125 mL min^{-1}. A "nitrogen knife" positioned immediately after the slot-die head was used to control the drying dynamics of the wet film. Following deposition, the films were annealed on a hot plate set to 100°C, placed beneath the tensioned substrate. Annealing was carried out for 80 min under ambient conditions at 30%–40% relative humidity.

After annealing, the inspection prototype was used to predict film thickness in-line, under the same illumination and imaging conditions employed during model training and validation. Thickness measurements were continuously acquired across regions of interest (ROIs) along a fixed inspection line. Each ROI was defined as a 5 × 5 pixel square, and thickness values were collected in real time as the annealed film advanced through the inspection zone with a web speed of 0.3 m min^{-1}.

Each predicted scan line was stored and added to a cumulative history, enabling the reconstruction of a full 2D thickness map of the film. The entire acquisition process was recorded and is provided as Supporting Information S1. To assess thickness uniformity, the map was segmented into 100 regions: 5 across the cross-web direction and 20 along the machine direction. Within each region, the mean thickness, coefficient of variation, and MAD were calculated and visualized. This segmentation enables real-time evaluation, enabling immediate decision-making based on coating quality.

Author Contributions

Juan Pablo Velasquez: Conceptualization, Methodology, Data curation, Formal analysis, Visualization, Investigation, Methodology, Writing – original draft. Juan José Patiño: Methodology, Visualization, Writing. Keony Jimenez: Conceptualization, Data curation, Writing. Santiago Mesa: Device fabrication, Writing. Milton Perez: Device fabrication, reviewing. Ershad Parvazian: Conceptualization, Methodology, Reviewing. Edwin Alexander Ramírez: Review & editing. Rafael Betancur: Conceptualization, Review & editing, Trystan Watson: Funding acquisition, Project administration, Writing – review & editing. Franklin Jaramillo: Funding acquisition, Project administration, Writing – review & editing.

Acknowledgements

The authors affiliated with the University of Antioquia gratefully acknowledge the financial support provided by the Colombian Government through the SGR project BPIN 2022000100012, as well as the EPSRC grant EP/X025217/1. The authors also acknowledge the support of VIPERLAB, which provided access to high-level infrastructures and resources that contributed to the development of this research.

Funding

The authors affiliated with the University of Antioquia gratefully acknowledge the financial support provided by the Colombian Government through the SGR project BPIN 2022000100012, as well as the EPSRC grant EP/X025217/1. The authors also acknowledge the support of VIPERLAB, which provided access to high-level infrastructures and resources that contributed to the development of this research.

Conflicts of Interest

The authors declare no conflicts of interest.

Data Availability Statement

The collected datasets (https://doi.org/10.34740/kaggle/dsv/12954226, https://doi.org/10.34740/kaggle/dsv/12954291), the model (https://github.com/KeonyJR/A-low-parameters-Deep-Learning-Model-for-Fault-Detection-of-PV-Modules-Using-Thermal-Images), and the Python code for profilometry extraction (https://github.com/jpvc7/Profilometry-Thickness-Extraction-Code-) used in this study are publicly available to the community.

References

1. M. A. Green, A. Ho-Baillie, and H. J. Snaith, "The Emergence of Perovskite Solar Cells," *Nature Photonics* 8, no. 7 (2014): 506–514, https://doi.org/10.1038/nphoton.2014.134.

2. H. Tsai, W. Nie, J.-C. Blancon, et al., "High-efficiency Two-dimensional Ruddlesden–Popper Perovskite Solar Cells," *Nature* 536, no. 7616 (2016): 312–316, https://doi.org/10.1038/nature18306.

3. J. Li, J. Dagar, O. Shargaieva, et al., "Ink Design Enabling Slot-Die Coated Perovskite Solar Cells with >22% Power Conversion Efficiency, Micro-Modules, and 1 Year of Outdoor Performance Evaluation," *Advanced Energy Materials* 13 (2023): 2203898, https://doi.org/10.1002/aenm.202203898.

4. J. W. Lee, S. Tan, S. I. Seok, Y. Yang, and N. G. Park, "Rethinking the A Cation in Halide Perovskites," *Science* 375, no. 6583 (2022): abj1186, https://doi.org/10.1126/science.abj1186.

5. M. Saliba, T. Matsui, K. Domanski, et al., "Incorporation of Rubidium Cations into Perovskite Solar Cells Improves Photovoltaic Performance," *Science* 354, no. 6309: 206–209, https://doi.org/10.1126/science.aah5557.

6. M. R. Filip, G. E. Eperon, H. J. Snaith, and F. Giustino, "Steric Engineering of Metal-Halide Perovskites with Tunable Optical Band Gaps," *Nature Communications* 5, no. 1 (2014): 5757, https://doi.org/10.1038/ncomms6757.

7. T. Wu, S. Mariotti, P. Ji, et al., "Self-Assembled Monolayer Hole-Selective Contact for Up-Scalable and Cost-Effective Inverted Perovskite Solar Cells," *Advanced Functional Materials* 34 (2024): 2316500, https://doi.org/10.1002/adfm.202316500.

8. C. Li, K. Zhang, S. Maiti, et al., "Tailoring the Dimensionality of 2D/3D Heterojunctions for Inverted Perovskite Solar Cells," *ACS Energy Letters* 9, no. 3 (2024): 779–788, https://doi.org/10.1021/acsenergylett.4c00045.

9. R. Azmi, D. S. Utomo, B. Vishal, et al., "Double-Side 2D/3D Heterojunctions for Inverted Perovskite Solar Cells," *Nature* 628, no. 8006 (2024): 93–98, https://doi.org/10.1038/s41586-024-07189-3.

10. Z. Zhang, H. Wang, T. J. Jacobsson, and J. Luo, "Big Data Driven Perovskite Solar Cell Stability Analysis," *Nature Communications* 13, no. 1 (2022): 7639, https://doi.org/10.1038/s41467-022-35400-4.

11. National Renewable Energy Laboratory *Best Research-Cell Efficiency Chart*, (National Renewable Energy Laboratory, 2026).

12. G. Yan, Y. Yuan, M. Kaba, and T. Kirchartz, "Visualizing Performances Losses of Perovskite Solar Cells and Modules: from Laboratory to Industrial Scales," *Advanced Energy Materials* 15, no. 3 (2025): 2403706, https://doi.org/10.1002/aenm.202403706.

13. F. Wang, Y. Han, D. Duan, C. Ge, H. Hu, and G. Li, "Recent Progress of Scalable Perovskite Solar Cells and Modules," *Energy Reviews* 1, no. 2 (2022): 100010, https://doi.org/10.1016/j.enrev.2022.100010.

14. J. Yan, T. J. Savenije, L. Mazzarella, and O. Isabella, "Progress and Challenges on Scaling up of Perovskite Solar Cell Technology," *Sustainable Energy & Fuels* 6, no. 2 (2022): 243–266, https://doi.org/10.1039/D1SE01045J.

15. M. Abbas, L. Zeng, F. Guo, M. Rauf, X.-C. Yuan, and B. Cai, "A Critical Review on Crystal Growth Techniques for Scalable Deposition of Photovoltaic Perovskite Thin Films," *Materials* 13, no. 21 (2020): 4851, https://doi.org/10.3390/ma13214851.

16. Y. Deng, C. H. Van Brackle, X. Dai, J. Zhao, B. Chen, and J. Huang, “Tailoring Solvent Coordination for High-Speed, Room-Temperature Blading of Perovskite Photovoltaic Films,” *Science Advances* 5, no. 12 (2019): aax7537, https://doi.org/10.1126/sciadv.aax7537.

17. C. S. Pathak, H. Choi, H. Kim, et al., “Recent Progress in Coating Methods for Large-Area Perovskite Solar Module Fabrication,” *Solar RRL* 8, no. 4 (2024): 2300860, https://doi.org/10.1002/solr.202300860.

18. A. Vijayan, M. B. Johansson, S. Svanström, U. B. Cappel, H. Rensmo, and G. Boschloo, “Simple Method for Efficient Slot-Die Coating of MAPbI$_3$ Perovskite Thin Films in Ambient Air Conditions,” *ACS Applied Energy Materials* 3, no. 5 (2020): 4331–4337, https://doi.org/10.1021/acsaem.0c00039.

19. H. Wang, Z. Qin, Y. Miao, and Y. Zhao, “Recent Progress in Large-Area Perovskite Photovoltaic Modules,” *Transactions of Tianjin University* 28, no. 5 (2022): 323–340.

20. S. Yuan, D. Zheng, T. Zhang, et al., “Scalable Preparation of Perovskite Films with Homogeneous Structure via Immobilizing Strategy for High-Performance Solar Modules,” *Nature Communications* 16, no. 1 (2025): 2052, https://doi.org/10.1038/s41467-025-57303-w.

21. K. Bochun and F. Yan, “Emerging Strategies for the Large-Scale Fabrication of Perovskite Solar Modules: from Design to Process,” *Energy & Environmental Science* 18 (2025): 3917–3954.

22. R. Keshavarzi, F. Hajisharifi, Z. Saki, et al., “Organic and Perovskite Solar Cells Based on Scalable Slot-Die Coating Technique: Progress and Challenges,” *Nano Today* 61 (2025): 102600, https://doi.org/10.1016/j.nantod.2024.102600.

23. D. Beynon, E. Parvazian, K. Hooper, et al., “All-Printed Roll-to-Roll Perovskite Photovoltaics Enabled by Solution-Processed Carbon Electrode,” *Advanced Materials* 35, no. 16 (2023): 2208561, https://doi.org/10.1002/adma.202208561.

24. Z. Fang, Y. Yan, C. Li, X. Luo, and P. Zhou, “Bubble Defect Generation Mechanism in Slot Die Coating of High-Viscosity Fluids,” *ACS Applied Materials & Interfaces* 16, no. 9 (2024): 11890–11900, https://doi.org/10.1021/acsami.3c18459.

25. K. Geistert, R. Pappenberger, P. Scharfer, et al., “Spatially Regulated Gas Flow Control for Batch-Drying of Large Area Slot-Die-Coated Perovskite Thin Films,” *Advanced Energy Materials* 15 (2025): 2500923, https://doi.org/10.1002/aenm.202500923.

26. R. Patidar, D. Burkitt, K. Hooper, D. Richards, and T. Watson, “Slot-Die Coating of Perovskite Solar Cells: An Overview,” *Materials Today Communications* 22 (2020): 100808, https://doi.org/10.1016/j.mtcomm.2019.100808.

27. A. Giuri, S. Masi, A. Listorti, et al., “Polymeric Rheology Modifier Allows Single-Step Coating of Perovskite Ink for Highly Efficient and Stable Solar Cells,” *Nano Energy* 54 (2018): 400–408, https://doi.org/10.1016/j.nanoen.2018.10.039.

28. S. Valsalakumar, A. Roy, T. K. Mallick, J. Hinshelwood, and S. Sundaram, “Mesoporous TiO$_2$-Layer’s Rheological Impact on the Perovskite Solar Cell Performance,” *Materials Letters* 337 (2023): 133960, https://doi.org/10.1016/j.matlet.2023.133960.

29. G. Shi, Z. Huang, R. Qiao, et al., “Manipulating Solvent Fluidic Dynamics for Large-Area Perovskite Film-Formation and White Light-Emitting Diodes,” *Nature Communications* 15, no. 1 (2024): 1066, https://doi.org/10.1038/s41467-024-45488-5.

30. A. Agresti, F. Di Giacomo, S. Pescetelli, and A. Di Carlo, “Scalable Deposition Techniques for Large-Area Perovskite Photovoltaic Technology: A Multi-Perspective Review,” *Nano Energy* 122 (2024): 109317, https://doi.org/10.1016/j.nanoen.2024.109317.

31. K. Wang, C. Wu, Y. Hou, et al., “A Nonionic and Low-Entropic MA(MMA)$_n$PbI$_3$-Ink for Fast Crystallization of Perovskite Thin Films,” *Joule* 4, no. 3 (2020): 615–630, https://doi.org/10.1016/j.joule.2020.01.004.

32. E. Pineda De La O, N. Alhazmi, S. J. Ebbens, and A. D. F. Dunbar, “Influence of Additives on the In Situ Crystallization Dynamics of Methyl Ammonium Lead Halide Perovskites,” *ACS Applied Energy Materials* 4, no. 2 (2021): 1398–1409.

33. Z. Hu, Z. Wang, and P. Gao, “Advancements in Scaling up Perovskite Solar Cells: from Small-Area Devices to Large-Scale Modules,” *Chemphyschem* 25, no. 22 (2024): 202400587, https://doi.org/10.1002/cphc.202400587.

34. L. A. Castriotta, M. A. Uddin, H. Jiao, and J. Huang, “Transition of Perovskite Solar Technologies to Being Flexible,” *Advanced Materials* 37, no. 8 (2025): 2408036, https://doi.org/10.1002/adma.202408036.

35. K. Maize, Y. Mi, M. Cakmak, and A. Shakouri, “Real-Time Metrology for Roll-To-Roll and Advanced Inline Manufacturing: A Review,” *Advanced Materials Technologies* 8, no. 2 (2023): 2200173, https://doi.org/10.1002/admt.202200173.

36. H. C. Weerasinghe, N. Macadam, J.-E. Kim, et al., “The First Demonstration of Entirely Roll-to-Roll Fabricated Perovskite Solar Cell Modules under Ambient Room Conditions,” *Nature Communications* 15, no. 1 (2024): 1656, https://doi.org/10.1038/s41467-024-46016-1.

37. M. Wagner, A. Distler, V. M. Le Corre, et al., “Cutting “Lab-to-fab” Short: High Throughput Optimization and Process Assessment in Roll-to-roll Slot Die Coating of Printed Photovoltaics,” *Energy & Environmental Science* 16, no. 11 (2023): 5454–5463, https://doi.org/10.1039/D3EE01801F.

38. E. Parvazian and T. Watson, “The Roll-to-Roll Revolution to Tackle the Industrial Leap for Perovskite Solar Cells,” *Nature Communications* 15 (2024): 3983, https://doi.org/10.1038/s41467-024-48518-4.

39. J. Petermann, B. Hacene, M. Gholipoor, et al., “Advanced Photoluminescence Imaging Method for Robust and Scalable Perovskite Quality Monitoring in Monolithic Tandem Solar Cells,” *Solar RRL* 9 (2025): 202500074.

40. B. Hacene, F. Laufer, S. Ternes, et al., “Intensity Dependent Photoluminescence Imaging for In-Line Quality Control of Perovskite Thin Film Processing,” *Advanced Materials Technologies* 9, no. 11 (2024): 2301279, https://doi.org/10.1002/admt.202301279.

41. F. Zhu, K. Xie, L. Quan, and D. Gan, “Multispectral Compressive Light Beam Induced Current Method for Photovoltaic Cell Assessment,” *Solar Energy* 275 (2024): 112621.

42. K. Frohna, C. Chosy, A. Al-Ashouri, et al., “The Impact of Interfacial Quality and Nanoscale Performance Disorder on the Stability of Alloyed Perovskite Solar Cells,” *Nature Energy* 10, no. 1 (2025): 66–76, https://doi.org/10.1038/s41560-024-01660-1.

43. C. C. Ahia and E. L. Meyer, “Advances in the Use of Atomic Force Microscopy as a Diagnostic Tool for Solar Cells Characterization: from Material Design to Device Applications,” *physica status solidi* 221, no. 3 (2024): 2300293.

44. Y. Gao, C. Liu, M. He, et al., “Efficient and Stable Perovskite Solar Modules Enabled by Inhibited Escape of Volatile Species,” *Advanced Materials* 36, no. 8 (2024): 2309310, https://doi.org/10.1002/adma.202309310.

45. I. J. Djeukeu, J. Horn, M. Meixner, E. Wagner, S. W. Glunz, and K. Ramspeck, “Subcell-Resolved Electroluminescence Imaging of Monolithic Perovskite/Silicon Tandem Solar Cell for High-Throughput Characterization,” *Solar RRL* 8, no. 19 (2024): 2400469, https://doi.org/10.1002/solr.202400469.

46. J. P. Velásquez, E. A. Ramírez, A. Flórez, et al., “Reaching Highly Uniform Perovskite Ink Flow from a Slot-Die Head toward Printed Solar Cells,” *Advanced Engineering Materials* 2201561 (2023): 1–7, https://doi.org/10.1002/adem.202201561.

47. E. A. Ramírez, J. P. Velásquez, A. Flórez, J. F. Montoya, R. Betancur, and F. Jaramillo, “Blade-Coated Solar Minimodules of Homogeneous Perovskite Films Achieved by an Air Knife Design and a Machine Learning-Based Optimization,” *Advanced Engineering Materials* 2200964 (2022): 1–9, https://doi.org/10.1002/adem.202200964.

48. R. Singh, R. Kashyap, and A. Kumar, “Prominent Solution for Solar Panel Defect Detection Using AI-Based Computer Vision Tech-

nology with IoT Sensors in the Solar Panel Manufacturing Industry," *International Journal of Information Technology* (2024): 1–17.

49. T. Kropp, M. Schubert, and J. H. Werner, "Quantitative Prediction of Power Loss for Damaged Photovoltaic Modules Using Electroluminescence," *Energies* 11, no. 5 (2018): 1172, https://doi.org/10.3390/en11051172.

50. S. Deitsch, V. Christlein, S. Berger, et al., "Automatic Classification of Defective Photovoltaic Module Cells in Electroluminescence Images," *Solar Energy* 185 (2019): 455–468, https://doi.org/10.1016/j.solener.2019.02.067.

51. L. W. T. Ng, N. G. An, L. Yang, et al., "A Printing-Inspired Digital Twin for the Self-Driving, High-Throughput, Closed-Loop Optimization of Roll-to-Roll Printed Photovoltaics," *Cell Reports Physical Science* 5, no. 6 (2024): 102038.

52. N. Taherimakhsousi, M. Fievez, B. P. MacLeod, et al., "A Machine Vision Tool for Facilitating the Optimization of Large-Area Perovskite Photovoltaics," *npj Computational Materials* 7, no. 1 (2021): 190, https://doi.org/10.1038/s41524-021-00657-8.

53. M. Harth, L. Vesce, I. Kouroudis, M. Stefanelli, A. D. Carlo, and A. Gagliardi, "Optoelectronic Perovskite Film Characterization via Machine Vision," *Solar Energy* 262 (2023): 111840, https://doi.org/10.17632/zt2j5j4v44.1.

54. F. Laufer, M. Götz, and U. W. Paetzold, "Deep Learning for Augmented Process Monitoring of Scalable Perovskite Thin-Film Fabrication," *Energy & Environmental Science* 18, no. 4 (2025): 1767–1782, https://doi.org/10.1039/d4ee03445g.

55. D. Zheng, F. Raffin, P. Volovitch, and T. Pauporté, "Control of Perovskite Film Crystallization and Growth Direction to Target Homogeneous Monolithic Structures," *Nature Communications* 13, no. 1 (2022): 6655, https://doi.org/10.1038/s41467-022-34332-3.

56. K. A. Bush, N. Rolston, A. Gold-Parker, et al., "Controlling Thin-Film Stress and Wrinkling during Perovskite Film Formation," *ACS Energy Letters* 3, no. 6 (2018): 1225–1232, https://doi.org/10.1021/acsenergylett.8b00544.

57. S. Ternes, T. Börnhorst, J. A. Schwenzer, et al., "Drying Dynamics of Solution-Processed Perovskite Thin-Film Photovoltaics: In Situ Characterization, Modeling, and Process Control," *Advanced Energy Materials* 9, no. 39 (2019): 1901581.

58. D. Burkitt, R. Swartwout, J. McGettrick, et al., "Acetonitrile Based Single Step Slot-Die Compatible Perovskite Ink for Flexible Photovoltaics," *RSC Advances* 9, no. 64 (2019): 37415–37423, https://doi.org/10.1039/c9ra06631d.

59. D. Burkitt, R. Patidar, P. Greenwood, et al., "Roll-to-roll Slot-die Coated P–I–N Perovskite Solar Cells Using Acetonitrile Based Single Step Perovskite Solvent System," *Sustainable Energy & Fuels* 4, no. 7 (2020): 3340–3351, https://doi.org/10.1039/D0SE00460J.

60. K. J. Restrepo. A-low-parameters-Deep-Learning-Model-for-Fault-Detection-of-PV-Modules-Using-Thermal-Images, Github, (2024), https://github.com/KeonyJR/A-low-parameters-Deep-Learning-Model-for-Fault-Detection-of-PV-Modules-Using-Thermal-Images.

61. K. Jimenez, J. B. Cano, and E. A. L. Velilla, "Deep Learning Model for Fault Detection of PV Modules Using Thermal Images," *Solar Energy* 303 (2026): 114120.

62. O. Ronneberger, P. Fischer, and T. Brox, "U-Net: Convolutional Networks for Biomedical Image Segmentation," in *International Conference on Medical Image Computing and Computer-Assisted Intervention*, (Springer, 2015), pp 234–241.

63. G. Huang, Z. Liu, L. Van Der Maaten, and K. Q. Weinberger, "Densely Connected Convolutional Networks," in *Proceedings of the IEEE Conference on Computer Vision and Pattern Recognition*, (IEEE, 2017), pp 4700–4708.

64. J. Wang, K. Sun, T. Cheng, et al., "Deep High-Resolution Representation Learning for Visual Recognition," *IEEE Transactions on Pattern Analysis and Machine Intelligence* 43, no. 10 (2020): 3349–3364, https://doi.org/10.1109/TPAMI.2020.2983686.

Supporting Information

Additional supporting information can be found online in the Supporting Information section.

Supporting File 1: aelm70419-sup-0001-SuppMat.docx.

Supporting File 2: aelm70419-sup-0002-VideoFile.mp4.